

A Search for Technosignatures toward the Galactic Centre at 150 MHz

Chenoa D. Tremblay^{1,2}*, Danny C. Price³, and Steven J. Tingay³

¹CSIRO, Space and Astronomy, Australian Telescope National Facility, PO Box 1130, Bentley WA 6102, Australia

²SETI Institute, Mountain View, CA 94043, USA

³International Centre for Radio Astronomy Research, Curtin University, Bentley, WA 6102, Australia

Abstract

This paper is the fourth in a series of low-frequency searches for technosignatures. Using the Murchison Widefield Array over two nights we integrate 7 hours of data toward the Galactic Centre (centred on the position of Sagittarius A*) with a total field-of-view of 200 deg². We present a targeted search toward 144 exoplanetary systems, at our best yet angular resolution (75 arcseconds). This is the first technosignature search at a frequency of 155 MHz toward the Galactic Centre (our previous central frequencies have been lower). A blind search toward in excess of 3 million stars toward the Galactic Centre and Galactic bulge is also completed, placing an equivalent isotropic power limit $<1.1 \times 10^{19}$ W at the distance to the Galactic Centre. No plausible technosignatures are detected.

Keywords: planets and satellites: detection – radio lines: planetary systems – instrumentation:interferometers – techniques: spectroscopic

1 INTRODUCTION

The prevalence of life beyond Earth is a central and unanswered question within astrobiology. The search for extraterrestrial intelligence (SETI) seeks to answer this question via detection of “technosignatures”, artificial signals that indicate the existence of technologically-capable societies (see review by [Tarter, 2001](#)). On Earth, low-frequency radio signals, like those used by FM radio, are a ubiquitous choice for communications. Many astrophysical processes give rise to low-frequency radio emission, and as such numerous large and sensitive low-frequency radio telescopes have been built, including the current-generation Murchison Widefield Array (MWA, [Tingay et al., 2013](#); [Wayth et al., 2018](#)), Long Wavelength Array (LWA, [Ellingson et al., 2009](#)), Low-Frequency Array (LOFAR, [van Haarlem et al., 2013](#)) and Giant Metrewave Radio Telescope (GMRT, [Gupta et al., 2017](#)). The existence of both powerful transmitters and sensitive receivers at low frequencies—both of which emerged early in the history of radio engineering—motivates low-frequency technosignature searches by providing an example class of engineered signals to search for, and instruments with which to do so.

This paper is the fourth in a series of papers detailing

SETI observations with the Murchison Widefield Array (MWA, [Tingay et al., 2013](#); [Wayth et al., 2018](#)), the details of which are summarised in Table 1. The MWA offers two advantages over other SETI searches; its large field of view and the low frequency range. These searches of ~ 400 – 600 square degrees, are some of the largest published surveys, although no candidate technosignature signals were detected above the detection limits. Both [Garrett et al. \(2017\)](#) and more recently [Houston et al. \(2021\)](#) have discussed the benefits of using aperture arrays like MWA for efficiently completing an all-sky SETI survey. [Houston et al. \(2021\)](#) outlines strategies of SETI searches from past, present, and future and suggests that if a receiver and transmitter are aligned in “...space, time and frequency, with adequate receive power, a detection can occur.” They suggest that unless there is a compelling reason to only search stellar regions, wide-field searches of any signal of unknown origin are required.

However, before we get to all-sky technosignature searches there are a number of computational challenges to overcome and these surveys have provided insight on how to accomplish this goal with an aperture array. While each of the MWA SETI publications follows a similar processing and search approach, our data analysis techniques have been gradually and significantly improved. The observations toward Orion represented an

*astrochenoa@gmail.com

improvement in imaging techniques and source finding. In the observations toward Vela, the data were collected with an updated “Phase II” array, increasing the spatial resolution by more than a third (3 arc minutes down to 1 arc minute).

In addition to the large field-of-view offered by the MWA, our surveys also represent the first published low radio frequency searches (see Figure 1). Since we don’t know what frequency another technologically advanced civilisation might broadcast or operate at, there is no reason to ignore available search space. There are additional motivations for low-frequency as well. Sullivan et al. (1978) suggested that the FM radio broadcasting stations of the world represents the greatest power per hertz in the radio band and this was further explored by Loeb & Zaldarriaga (2007). Overall, there is growing support for broadening the frequency range searched for technosignatures to lower frequencies. For example, Houston et al. (2021) find that, according to several detection optimisation metrics, SETI surveys should be undertaken down into the hundreds of megahertz frequency range.

In this survey we utilise the procedures developed in our search toward Vela to search 200 deg² toward the centre of our Galaxy but at a higher frequency of 155 MHz. This survey maintains the higher spatial resolution we obtained toward Vela, but encompasses the largest population of known exoplanets than across our previous surveys.

1.1 The Galactic Centre

The Galactic Centre (GC) is a prime SETI target as the line of sight toward the GC has the largest integrated count of Galactic stars for any direction. Here, we outline some arguments favouring and disfavouring the GC as a region where intelligent life may reside; however, we note that direct observational evidence remains the only method capable of proving the existence of life beyond Earth.

The high density of stars within the GC means that cataclysmic events such as stellar supernovae and magnetar flares are more likely to impact exoplanets within the GC, potentially destroying any life on their surface. Based on these factors, Lineweaver et al. (2004) identify a ‘Galactic habitable zone’ as an annular region between 7–9 kpc from the GC. Interactions due to close stellar flybys—more common within the dense GC—are also expected to damage planetary disks (Lineweaver et al., 2004; Jiménez-Torres et al., 2013); however, on longer timescales this could be advantageous to habitability. Despite these factors, modelling by Gowanlock et al. (2011) finds a majority of planets that may support complex life are found toward the inner Galaxy (less than 1 kpc from the Galactic Centre). Morrison & Gowanlock (2015) extend this model to include intelligent life, and

also find higher probability within the inner Galaxy. Gajjar et al. (2021) update the model of Gowanlock et al. (2011) to include the galactic bulge within the radius $R < 2.5$ kpc, again finding the fraction of stars with a habitable planet is greatest in the inner regions of the Galaxy. Modelling by Cai et al. (2021), which includes factors such as abiogenesis (the idea that life arose from nonlife), evolutionary timescales, and self-annihilation also find a higher likelihood of intelligent life emerging in the Galactic inner disk (defined here as $R \leq 8$ kpc), with peak likelihood at an annulus 4 kpc from the GC.

Separate to the propensity of life to emerge, the GC’s high stellar density may be advantageous to the growth of advanced space-faring societies. Such societies are likely to be capable of producing technosignatures detectable across large distances. First discussed in Newman & Sagan (1981), diffusion of advanced societies across the Milky way is accelerated in areas of high stellar density. Di Stefano & Ray (2016) suggest that the close proximity of stars within dense globular clusters is favourable to the diffusion of space-faring societies. Modelling by Carroll-Nellenback et al. (2019) also suggests that high stellar density provides a front for settlements to rapidly expand from. Nevertheless, dust grains, gas and cosmic rays all pose hazards to interstellar travels, making the GC harder to traverse (Lacki, 2021). The GC can also be considered a natural cynosure, or ‘Schelling point’ within the Milky Way: an optimal location to place a transmitter to maximise the chances of its detection (Gajjar et al., 2021).

Despite arguments that motivate SETI searches of the GC, only a handful of observations have been published. In 1981, the Westerbork Synthesis Radio Telescope was used to search for narrow band pulsating beacons in the GC (Shostak & Tarter, 1985). Our previous observations (Paper 1, Tingay et al., 2016) searched toward 38 known exoplanets at a 10 kHz resolution in 2 hours of data. As part of the Breakthrough Listen search for intelligent life, the GC is being surveyed using the Robert C. Byrd Green Bank Telescope (GBT) and Parkes 64 m telescope to cover 0.7–93 GHz (Worden et al., 2017; Gajjar et al., 2021). Our observations, which are at lower frequency, complement the Breakthrough Listen search. Both Parkes and Green Bank are large single-dish telescopes with wide-bandwidth receivers. Interferometers, such as the MWA, offer wider fields of view and much better spatial resolution, giving improved signal localisation and radio frequency interference (RFI) rejection. However, compared to single-dish telescopes, interferometers have higher ingest data rates and require more demanding signal processing systems; consequently, their instantaneous bandwidth and spectral resolution are generally more constrained than single-dish instruments. As such, single-dish and interferometric approaches to technosignatures are complementary.

As shown in Figure 2 (Section 3.1), the known exo-

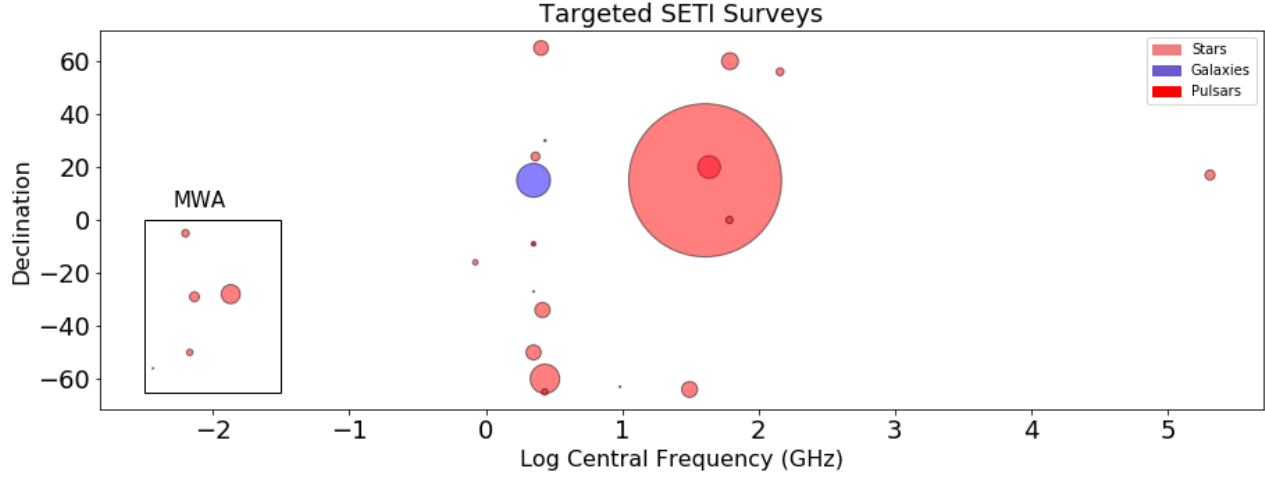


Figure 1. A plot showing all targeted SETI searches published to date, as listed in <https://technosearch.seti.org/radio-list> and [Enriquez et al. \(2017\)](#). The x-axis is the central frequency of the survey and the y-axis represents the median declination the survey covered. The colour of the circle represents the type of objects observed in the SETI survey and the size of the bubble is representative of the number of sources targetted in the survey. This does not cover blind searches toward stars with no known exoplanets.

Table 1 Parameters of previous MWA SETI surveys.

	Phase centre (J2000)	Phase center l,b (deg)	Freq. (MHz)	FoV (deg ²)	RMS _{min} (Jy/beam)	EIRP _{min} 10 ¹³ (W)	Exoplanets Known
Galactic Centre Tingay et al. 2013	Phase I MWA 17h45m40s −29d00m28s	0, 0	103–133	400	0.45	<4	38
Orion Tingay et al. 2018	Phase I MWA 05h35m17s −05d23m28s	196, −15	99–122	625	0.28	<1	22
Vela Tremblay & Tingay 2020	Phase I MWA 08h35m27s −45d12m19s	264, −5	98–128	400	0.034	<0.6	6
Galactic Centre This work	Phase II MWA 17h45m40s −29d00m28s	0, 0	139–169	200	0.14	< 27	144

planets in this survey are distributed along either side of the Galactic plane (plus and minus longitude centred along $b=0$). Microlensing is the most common method of detection and, as such, this population represents a population of planets significantly more distant than some of our previous surveys.

2 OBSERVATIONS

The Murchison Widefield Array (MWA; [Tingay et al. 2013](#)) is a low-frequency interferometer operating between 70 and 300 MHz at the Murchison Radio-astronomy Observatory in Western Australia. In 2018, the telescope was upgraded to the ‘‘Phase II’’ array ([Wayth et al., 2018](#)), doubling the number of aperture array tiles from 128 to 256 and approximately doubling the maximum baseline from 3 km to 5.5 km, of which 128 tiles are correlated at one time. These observations use the extended ‘‘long base-line array’’ with baselines between ~ 22 m and 5.5 km.

Observations of the Galactic Centre, centred on J2000 coordinates 17:45:40.04 $-29:00:28$, were taken during 5–7 September 2020 for a total of 10.5 hours and are summarised in [Table 2](#). The observations were taken when the Galactic Centre was low on the horizon¹, so only 7 hours of the most sensitive observations were processed. The data were calibrated from 2-minute observations of Hercules A each night and processed as described in [Tremblay et al. \(2020\)](#). To image these observations we used WSCLEAN version 2.9.2 with Briggs weighting of -1 . Due to the large volume of these data, we did not process using other weightings. This weighting improves our point-source sensitivity to reduce the potential effects of beam dilution over previous publications. These settings produced a cube with a field-of-view (FOV) of 200 square degrees and a synthesised beam of 75×67 arc seconds. Based on the bandpass solutions, three of the 128 tiles were flagged for every observation.

The MWA uses a two-stage polyphase filter-bank which channelises the data into 24×1.28 MHz ‘‘coarse’’ frequency channels which are then further divided into 128×10 kHz ‘‘fine’’ frequency channels resulting in 3072 (10 kHz-wide) spectral channels. Each of the 85 5-minute observations were imaged independently using WSCLEAN ([Offringa & Smirnov, 2017](#)) and a Stokes I primary beam model was created using the simulation-based Full Embedded Element (FEE) model of [Sokolowski et al. \(2017\)](#) for each of 24 coarse channels. The creation of the model, taking into account the phase centre and other individual observational parameters

¹The MWA observations are obtained through competitive time allocation and when the observations happen are based on scientific priorities and work around maintenance schedules. Therefore preferential observational time when the Galactic Centre was closer to zenith was not available.

Table 2 MWA Observing Parameters

Parameter	Value
Central frequency	154.4 MHz
Total bandwidth	30.72 MHz
Number of imaged channels	2400
Number Channels used in Search	2280
Channel separation	10 kHz
Synthesized beam FWHM*	$83'' \times 67''$
Imaged Region	200 sq. deg.
Phase centre of image (J2000)	17h45m40s $-29d00m28s$
Total Integration Time	7 hours

*Full Width at Half Maximum (FWHM)

in the metadata, was created using code by [Morgan & Galvin \(2021\)](#). The primary beam model was applied to the 100 fine frequency channels imaged² within each coarse channel to create primary beam corrected spectral channel images. The images were then stacked together into a three-dimensional data cube for each observation, which is then time-averaged together using inverse variance weighting. After correction, the flux density error was determined by comparison to the Molonglo Reference Catalogue (MRC; [Large et al. 1981](#)) which was scaled down to our frequency using a spectral index of -0.83 , as described in detail in [Hurley-Walker et al. \(2017\)](#). The error across the field was 9 ± 20 mJy.

Radio Frequency Interference (RFI) was flagged in two stages in the u, v, w (visibility) domain. First, each 5-minute observation was flagged using a statistical technique invoked by AOFFLAGGER ([Offringa et al., 2015](#)) and is a standard option for data downloaded through the All-Sky Virtual Observatory. Secondly, a baseline flagging algorithm which flagged amplitudes in u, v, w of baselines that were higher than three times the standard deviation³. This flagged $< 1-3\%$ of the baselines. In previous work ([Tremblay et al., 2020](#)), strong FM band interference required a third-stage image-based filtering to flag channels where RFI was detected in a large fraction of pixels; this third-stage flagging was not required for these data. An example spectrum is shown in [Figure 4](#).

The ionosphere can create an astrometric shift in the sources which is more pronounced at lower frequencies. The estimated source position error is estimated in the final composite image by comparing to the MRC. After correction, the systematic spatial error in a fully integrated continuum image was $+5 \pm 8$ arcseconds in right ascension and $+22 \pm 5$ arcseconds in declination. The ratio of point source flux density and peak intensity is

²Only 100 of the 128 fine frequency channels in each coarse channel were imaged to avoid channels were suffer from instrumental aliasing.

³https://gitlab.com/Sunmish/piip/blob/master/ms_flag_by_uvdist.py

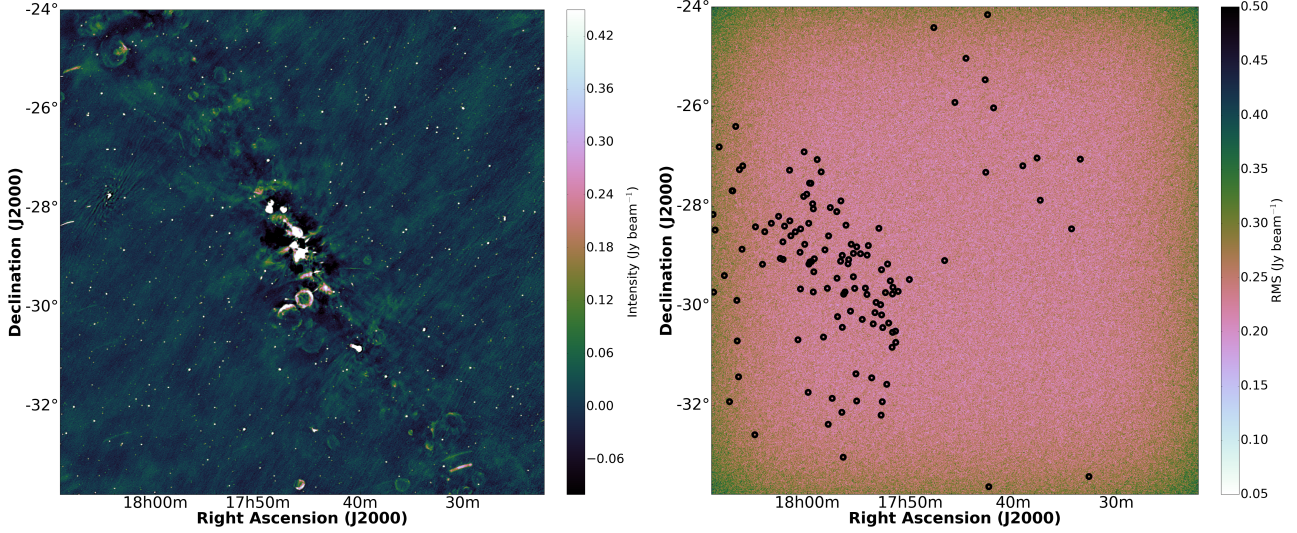


Figure 2. Continuum image of the Galactic Plane in ICRS Coordinates as viewed by the MWA at 155 MHz (left). The right-hand image is an image of the spectral RMS across the field, representative of the values extracted for the EIRP_{min} limits. The black circles are the positions of the known sources in The Extrasolar Planet Catalogue with solar mass less than 60 M_J (a limit set by the catalogue custodians), as summarised in Tables 3, 4, 5, and 6.

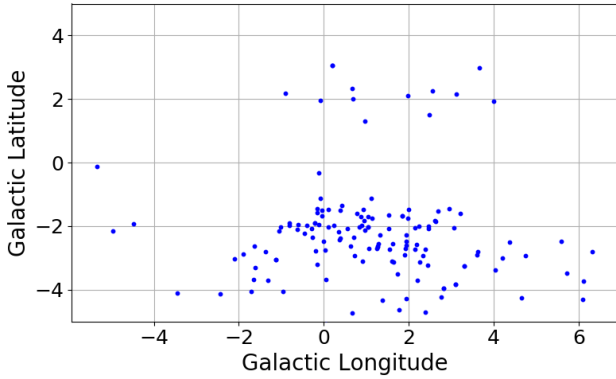


Figure 3. A plot of the sources listed in Tables 3, 4, 5, and 6 shown in Galactic Coordinates. As shown there are more sources distributed along the negative latitude which is likely a selection effect from the exoplanet survey axis fields.

1.1 ± 0.2 . This suggests that the ionospheric distortions are corrected for in these observations.

3 RESULTS

3.1 Known Exoplanets

The three-dimensional data cubes were each searched in frequency for 10 kHz (frequency resolution of the MWA) signals of non-astrophysical origin toward the 144 known exoplanets in our field. This list of exoplanets from the The Exoplanet Encyclopaedia⁴, represents an accumulated list of exoplanets with a mass limit of 60 M_J. In Tables 3, 4, and 5 we provide information on

⁴<http://exoplanet.eu/>

the planet designation, position, distance, planet mass, detection method, sensitivity limit as spectral variation in our data cube toward that position, and the equivalent isotropic power limit (EIRP). In Table 6 we provide the information of exoplanets in our sample which have no known distance, and therefore a limit on the EIRP could not be obtained.

Similar to our survey toward Vela (Tremblay & Tingay, 2020), we calculated the EIRP upper limit from the equation:

$$\text{EIRP}(W) < 1.12 \times 10^{12} S_{\text{rms}} R^2, \quad (1)$$

where S_{rms} is the RMS intensity value in Jy beam⁻¹ along the spectral frequency axis toward the source position and R is the distance to the stellar system in pc. Similar to our previous work, we assume a signal width of 10 kHz to match the frequency resolution of the MWA, and discuss in Section 4.1 about potential for spectral broadening when higher resolution is assumed. In these upper limits we assume that the signal optimally fills the 10 kHz channel width. If an artificial signal was an unresolved signal with a width between 1–10 kHz but constrained within the channel, the estimated EIRP would be underestimated by $10\text{kHz}/\Delta\nu t$, where $\Delta\nu t$ is the transmission bandwidth. We do not account for additional edge cases where a signal spans the channel gap between two fine frequency channels. We note that for the EIRP Limit toward the known sources we use a one sigma value for direct comparison with previous work and a 6 sigma limit for the blind search.

As shown in Figure 5, the majority of the stars containing exoplanets are near or below solar mass. It is also shown that the sample of known exoplanets have

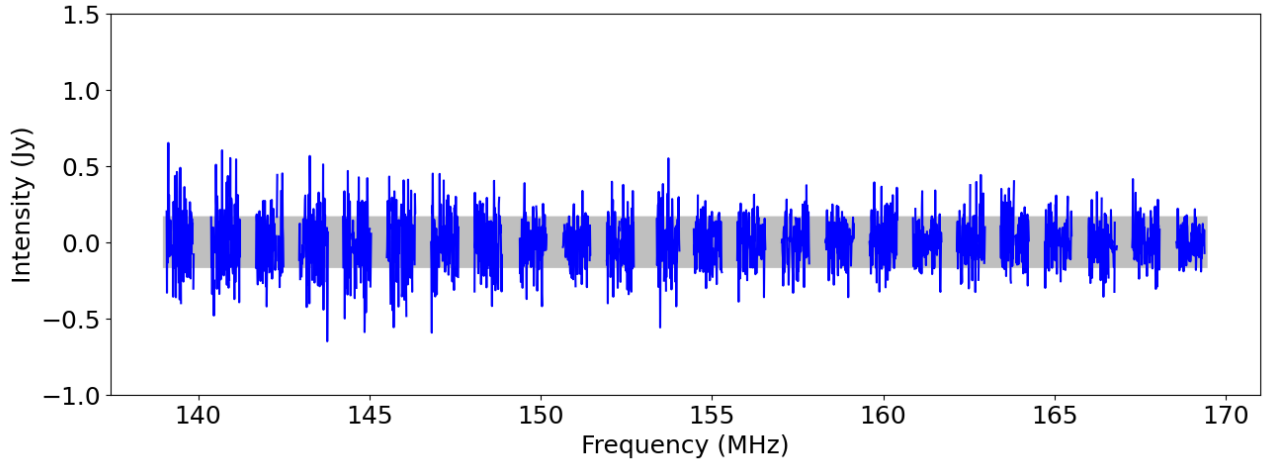


Figure 4. MWA spectrum, with a total integration time of 7 hours, at the position of KMT-2018-BLG-1292L b. Flagged channels and the edge channels which suffer from instrumental aliasing (see Section 2), are blanked out in the spectrum. The horizontal grey shaded region represents the $\pm 1\sigma$ RMS value used in Table 3.

a mean distance of 4.8 kpc, which is much farther than our sample of stellar objects we studied toward Vela or Orion.

3.2 Blind Signal Search

Each of the 2400 continuum-subtracted fine-channel (10 kHz) images, each containing 2000×2000 pixels, are independently searched using the source-finding software *AEGEAN* (Hancock et al., 2018). This is done using the function “slice”, to set which channel in the cube is searched, and setting a “seed clip” value of 5, in order to search the image for pixels with a peak intensity value greater than 5σ (where σ is set from an input RMS image). *AEGEAN* works by fitting Gaussian’s to the pixel data and applies a correction for the background⁵ to calculate the flux density for potential sources. This source-finding threshold has the goal of detecting all signals $>6\sigma$, which may not be pixel centred. Following this search, we found two signals over the $>10^9$ voxels searched. This is consistent with expected number of spurious signals within the data set. We therefore, do not detect any unknown emission sources.

In Tremblay & Tingay (2020) we used the *Gaia* catalogue to approximate the number of stars in the field toward Vela. However, due to the high dust extinction toward the Galactic Centre and Galactic bulge, optical surveys have difficulty detecting sources. Instead we use The GALACTICNUCLEUS Survey (GNS; Nogueras-Lara et al. 2018, 2019) which observes the J, K, and H infrared emission of 6000 pc^2 (0.3 deg^2) around the Galactic Centre, Galactic Bulge, and surrounding area. In their 49 independent pointings using the European

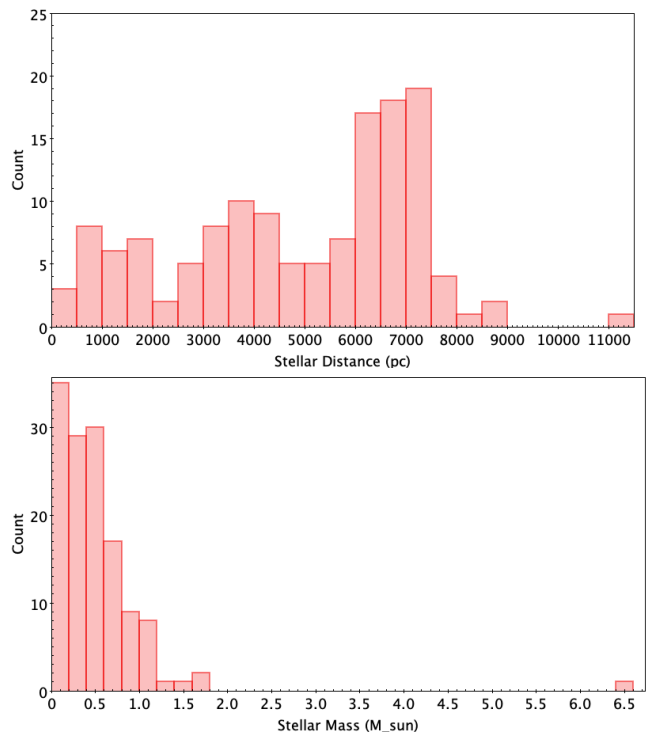


Figure 5. Summary of the stellar parameters of the known sources in the exoplanet catalogue. As shown most exoplanets are around a solar mass or less and the distances are distributed up to 9 kpc.

⁵The background is defined by the 50th percentile of flux distribution in a zone 30 times the size of the synthesised beam.

Table 3 Known exoplanets in the survey field, from the exoplanet catalog: <http://exoplanet.eu/>

Designation	RA (J2000) (deg.)	Dec (J2000) (deg.)	Distance (pc)	MSin(i) (M_J^a)	Period (days)	Detection method ^b	1σ RMS (Jy/beam)	EIRP ^c <10 ¹³ (W)
HD 164604 b	270.779	-28.561	39.4		641.47	RV	0.16	27.3
HD 165155 b	271.488	-29.917	64.98		434.50	RV	0.16	77.9
OGLE-2009-BLG-151L b	268.592	-29.056	390	7.50		Micro	0.14	2454
OGLE-2015-BLG-0954L b	270.183	-28.661	600	4.40		Micro	0.15	6029.8
MOA-2007-BLG-192L b	272.017	-27.150	700	0.01		Micro	0.18	10127.2
OGLE-2018-BLG-0532 b	269.983	-28.998	790	0.02		Micro	0.14	10117.6
MOA-2011-BLG-274 b	268.675	-28.916	800	0.80		Micro	0.15	10679.2
MOA-2010-BLG-328L b	269.496	-30.715	810	0.03		Micro	0.15	10922.4
OGLE-2017-BLG-1434L b	268.280	-30.246	860	0.01		Micro	0.15	12252.9
OGLE-2019-BLG-0960 b	274.013	-25.773	880	0.01		Micro	0.16	13601.5
OGLE-2013-BLG-0341L b	268.029	-29.846	911	0.01		Micro	0.14	13511.1
OGLE-2017-BLG-1522L b	270.321	-28.462	990	0.75		Micro	0.15	16405.6
OGLE-2013-BLG-0578L b	269.999	-29.735	1160	34.00		Micro	0.15	22762.2
OGLE-2016-BLG-1227 b	265.596	-33.760	1210	0.79		Micro	0.18	29124.6
KMT-2020-BLG-0414 b	271.917	-28.485	1220	0.00		Micro	0.18	29895.4
KMT-2020-BLG-0414 c	271.917	-28.485	1220	23.30		Micro	0.18	29895.4
OGLE-2014-BLG-0257L b	270.450	-28.262	1250	36.00		Micro	0.15	26529.6
OGLE-2012-BLG-0563L b	271.491	-27.712	1300	0.39		Micro	0.17	32042.1
OGLE-TR-10 b	267.867	-29.876	1500	0.68	3.10	PT	0.15	37511
OGLE-TR-56 b	269.146	-29.539	1500	1.30	1.21	PT	0.14	36541.1
OGLE-2006-109L b	268.146	-30.088	1510	0.73	1790.00	Micro	0.15	38090.3
OGLE-2006-109L c	268.146	-30.088	1510	0.27	4931.00	Micro	0.15	38090.3
OGLE-2014-BLG-1186L b	265.500	-34.288	1700	0.14		Micro	0.17	55313.1
OGLE-2012-BLG-0358L b	265.696	-24.261	1760	1.85		Micro	0.17	60509.2
OGLE-2011-BLG-0420L b	267.733	-29.825	1990	9.40		Micro	0.15	66967.7
OGLE-2014-BLG-0676L b	268.104	-30.548	2220	3.09		Micro	0.15	82461.9
MOA-2010-BLG-477L b	271.529	-31.454	2300	1.50		Micro	0.16	95860.4
OGLE-2018-BLG-1269L b	269.692	-27.618	2560	0.69		Micro	0.15	109438
KMT-2018-BLG-0029 b	264.471	-27.985	2730	0.02		Micro	0.15	127423
OGLE-2007-BLG-349L (AB) b	271.350	-26.422	2760	0.25		Micro	0.17	143323
OGLE-2015-BLG-0966L b	268.754	-29.047	2900	0.07		Micro	0.15	138517
KMT-2018-BLG-1292L b	263.179	-33.521	2920	4.90		Micro	0.17	163666
OGLE-2012-BLG-0950L b	272.019	-29.732	3000	0.11		Micro	0.18	184790
OGLE-2013-BLG-0102L b	268.030	-31.691	3020	13.60		Micro	0.15	152114
OGLE-2016-BLG-1266L b	267.854	-29.742	3050	11.90		Micro	0.15	156131
OGLE-2013-BLG-0911L b	268.883	-29.254	3220	10.08		Micro	0.15	172151
KMT-2019-BLG-0842 b	268.458	-29.878	3320	10.28		Micro	0.15	184695
MOA-2010-BLG-117 b	271.957	-25.345	3400	0.51		Micro	0.19	249325
OGLE-2016-BLG-0613L (AB) b	269.263	-28.116	3410	4.18		Micro	0.15	193939
MOA-2013-BLG-605L b	269.679	-29.398	3600	0.07		Micro	0.15	221716
MOA-2008-BLG-379L b	269.704	-29.803	3600	4.10		Micro	0.15	215639
OGLE-2014-BLG-0124L b	270.621	-28.396	3600	0.64		Micro	0.15	221489
OGLE-2019-BLG-0954L b	267.913	-29.611	3630	14.20		Micro	0.15	223793
OGLE-2016-BLG-1067L b	273.205	-27.013	3730	0.43		Micro	0.16	246169
OGLE-2017-BLG-1375 b	269.154	-30.311	3790	10.33		Micro	0.15	236189
KMT-2019-BLG-1715 b	270.371	-28.777	3860	2.56		Micro	0.15	252963
OGLE-2013-BLG-0132L b	269.765	-28.421	3900	0.29		Micro	0.15	262897
OGLE-2016-BLG-1195L b	268.850	-30.207	3910	0.00		Micro	0.15	251866

^aMass of planet times the sine of orbit inclination, in Jupiter masses^bRV= Radial Velocity; I=Imaging; PT=Primary Transit; Micro= Microlensing^cEquivalent Isotropic Radiated Power using the specified 1σ limit

Table 4 Known exoplanets in the survey field, from the exoplanet catalog: <http://exoplanet.eu/>

Designation	RA (J2000) (deg.)	Dec (J2000) (deg.)	Distance (pc)	MSin(i) (M_J^a)	Period (days)	Detection method ^b	1σ RMS (Jy/beam)	EIRP ^c <10 ¹³ (W)
OGLE-2017-BLG-0604 b	267.892	-30.947	3950	0.51		Micro	0.15	257703
OGLE-2017-BLG-0896	264.879	-27.298	4000	19.00		Micro	0.15	264158
OGLE-2006-BLG-284 b	269.658	-29.137	4000	0.45		Micro	0.15	271097
OGLE-2012-BLG-0026L b	263.579	-27.143	4080	0.11		Micro	0.15	279574
OGLE-2012-BLG-0026L c	263.579	-27.143	4080	0.68		Micro	0.15	279574
OGLE-2011-BLG-0251L b	264.559	-27.136	4090	0.96		Micro	0.15	285529
OGLE-2005-169L b	271.521	-30.733	4100	0.04		Micro	0.17	318741
MOA-2007-BLG-197L b	271.771	-31.946	4170	41.00		Micro	0.18	344970
OGLE-2015-BLG-1649 b	271.204	-32.633	4230	2.54		Micro	0.17	346455
OGLE-2011-BLG-0265L b	269.450	-27.394	4380	0.88		Micro	0.15	327138
OGLE-2016-BLG-1469L b	271.946	-26.290	4500	13.60		Micro	0.19	425740
KMT-2017-BLG-0165L b	269.650	-28.134	4530	0.11		Micro	0.15	350648
OGLE-2017-BLG-0173L b	267.971	-29.271	4700	9.08		Micro	0.14	358783
OGLE-2014-BLG-1112L b	272.151	-28.666	4840	31.70		Micro	0.18	471270
OGLE-2012-BLG-0406L b	268.325	-30.471	4970	2.73		Micro	0.15	405029
OGLE-2015-BLG-1319L b	269.442	-32.472	5000	45.00		Micro	0.15	434763
OGLE-2017-BLG-0406 b	269.000	-29.863	5200	0.41		Micro	0.15	446318
OGLE-2003-BLG-235L b	271.317	-28.895	5200	2.60		Micro	0.16	481272
MOA-2012-BLG-006 b	270.442	-29.109	5300	8.40		Micro	0.15	477922
XTE J1807-294 b	271.752	-29.409	5500	14.50	0.03	Timing	0.17	585384
OGLE-2017-BLG-1049 b	269.533	-27.144	5670	5.53		Micro	0.15	535062
MOA-2009-BLG-387L b	268.463	-33.990	5700	2.60	1970.00	Micro	0.18	647709
OGLE-2017-BLG-0482 b	269.049	-30.528	5800	9.00		Micro	0.15	568344
OGLE-2018-BLG-0596 b	269.054	-29.199	5900	0.03		Micro	0.15	590643
OGLE-2007-BLG-368L b	269.108	-32.238	5900	0.07		Micro	0.15	601071
OGLE-2017-BLG-0373L b	269.329	-31.952	5900			Micro	0.15	599534
KMT-2016-BLG-0212 b	268.439	-29.087	6000			Micro	0.15	597719
OGLE-2014-BLG-1760L b	269.408	-28.963	6060	0.57		Micro	0.15	607185
KMT-2017-BLG-1038 b	266.171	-25.143	6100	2.40		Micro	0.15	644335
MOA-2009-BLG-319L b	271.742	-26.820	6100	0.21		Micro	0.17	729184
OGLE-2011-BLG-0173L b	269.317	-28.684	6200	0.19		Micro	0.15	644380
OGLE-2018-BLG-1428L b	265.550	-26.138	6220	0.77		Micro	0.15	661154
KMT-2016-BLG-1820 b	268.767	-29.517	6260	4.57		Micro	0.15	657715
OGLE-2018-BLG-0799 b	273.458	-25.486	6290	0.41		Micro	0.17	738527
UKIRT-2017-BLG-001 b	266.654	-29.211	6300	1.28		Micro	0.15	653360
OGLE-2013-BLG-1721L b	268.127	-30.293	6300	0.64		Micro	0.14	649382
OGLE-2014-BLG-1722L b	268.754	-31.469	6400	0.17		Micro	0.15	674633
OGLE-2014-BLG-1722L c	268.754	-31.469	6400	0.26		Micro	0.15	674633
MOA-2016-BLG-227L b	271.475	-27.714	6400	2.30		Micro	0.17	778603
KMT-2016-BLG-2605 b	269.825	-26.982	6421	0.77		Micro	0.15	696601
MOA-2010-BLG-353L b	271.304	-27.293	6430	0.27		Micro	0.17	775990
KMT-2016-BLG-2364 b	265.717	-27.436	6440	3.93		Micro	0.15	698233
OGLE-2018-BLG-0962	268.175	-32.309	6470	1.37		Micro	0.15	727124
OGLE-2005-390L b	268.579	-30.377	6500	0.02	3500.00	Micro	0.15	696976
OGLE-2016-BLG-0263L b	269.895	-31.819	6500	4.10		Micro	0.15	722133
KMT-2017-BLG-1146 b	269.104	-33.143	6600	0.85		Micro	0.16	773762
KMT-2016-BLG-1397 b	272.667	-24.858	6600	7.00		Micro	0.17	860151
OGLE-2012-BLG-0838 b	273.004	-25.712	6620	0.25		Micro	0.17	818145

^aMass of planet times the sine of orbit inclination, in Jupiter masses^bRV= Radial Velocity; I=Imaging; PT=Primary Transit; Micro= Microlensing^cEquivalent Isotropic Radiated Power using the specified 1σ limit

Table 5 Known exoplanets in the survey field, from the exoplanet catalog: <http://exoplanet.eu/>

Designation	RA (J2000) (deg.)	Dec (J2000) (deg.)	Distance (pc)	MSin(i) (M_J^a)	Period (days)	Detection method ^b	1σ RMS (Jy/beam)	EIRP ^c <10 ¹³ (W)
KMT-2016-BLG-1107 b	266.417	-26.032	6651	3.28		Micro	0.15	750943
OGLE-2015-BLG-1670L b	268.159	-28.552	6700	0.06		Micro	0.15	740142
OGLE-2012-BLG-0724L b	268.967	-29.819	6700	0.47		Micro	0.15	743775
KMT-2018-BLG-125L b	269.863	-27.878	6700	0.02		Micro	0.15	768189
MOA-2013-BLG-220L b	270.988	-28.455	6720	2.74		Micro	0.16	798259
OGLE-2016-BLG-1190L b	269.721	-27.614	6770	13.38	1223.60	Micro	0.15	778927
MOA-2016-BLG-319L b	268.742	-29.751	6800	0.62		Micro	0.15	771666
OGLE-2008-BLG-355L b	269.787	-29.241	6800	4.60		Micro	0.15	768759
OGLE-2019-BLG-1053L b	270.167	-27.342	6800	0.01		Micro	0.15	783133
MOA-2007-BLG-400L b	272.425	-29.224	6890	1.71		Micro	0.17	902075
OGLE-2013-BLG-1761L b	268.408	-28.895	6900	2.80		Micro	0.15	787994
MOA 2009-BLG-411L b	268.493	-29.749	6900	53.00		Micro	0.15	819836
MOA-bin-29 b	269.375	-29.737	6900	0.55		Micro	0.14	773905
MOA-2011-BLG-291 b	268.867	-29.171	7000	0.09		Micro	0.15	807552
KMT-2016-BLG-2142 b	268.113	-29.384	7010	15.49		Micro	0.15	830574
KMT-2019-BLG-0371 b	268.383	-31.555	7025	16.50		Micro	0.15	833111
KMT-2019-BLG-1953L b	269.117	-28.201	7040	0.59		Micro	0.15	844163
KMT-2019-BLG-1953L c	269.117	-28.201	7040	0.28		Micro	0.15	844163
OGLE-2015-BLG-1771L b	268.800	-28.863	7070	0.43		Micro	0.15	823398
OGLE-2018-BLG-0567L b	269.017	-27.987	7070	0.32		Micro	0.14	812416
KMT-2016-BLG-1836L b	268.250	-30.041	7100	2.20		Micro	0.15	847778
OGLE-2018BLG-1011L b	269.013	-29.083	7100	1.80		Micro	0.14	820430
OGLE-2018BLG-1011L c	269.013	-29.083	7100	2.80		Micro	0.14	820430
MOA-2015-BLG-337 a	271.949	-28.170	7100	9.80		Micro	0.18	1022880
MOA-2015-BLG-337 b	271.949	-28.170	7100	0.11		Micro	0.18	1022880
KMT-2019-BLG-1339 (OGLE-2019/BLG-1019 b)	265.742	-25.574	7150	12.20		Micro	0.15	869033
MOA-2012-BLG-505L b	268.142	-32.040	7210	6.70		Micro	0.15	895489
KMT-2018-BLG-0748 b	267.875	-30.646	7300	0.19		Micro	0.15	900185
OGLE-2017-BLG-1140L b	266.883	-24.523	7350	1.63		Micro	0.17	1009590
MOA-2011-BLG-262L b	270.096	-30.755	7350	0.06		Micro	0.15	899051
MOA-2011-BLG-028L b	270.858	-29.213	7380	0.09		Micro	0.16	964267
OGLE-2018-BLG-1185 b	269.792	-27.835	7400	0.03		Micro	0.15	912731
OGLE-2018-BLG-1700L b	269.954	-28.529	7600	4.40		Micro	0.15	966195
OGLE-2018-BLG-0677L b	268.750	-32.017	7700	0.01		Micro	0.15	1000070
MOA-2011-BLG-293L b	268.913	-28.477	7700	4.80		Micro	0.14	966263
MOA-2011-BLG-322L b	271.225	-27.221	7740	7.80		Micro	0.16	1107550
OGLE-2015-BLG-0051L b	269.663	-28.032	8200	0.72		Micro	0.14	1098900
SWEEPS-04 b	269.725	-29.189	8500	3.80	4.20	PT	0.14	1171210
SWEEPS-11 b	269.763	-29.198	8500	9.70	1.80	PT	0.15	1236990
XTE J1751-305 b	267.806	-30.623	11000	27.00	0.03	Timing	0.15	2034430

^aMass of planet times the sine of orbit inclination, in Jupiter masses^bRV= Radial Velocity; I=Imaging; PT=Primary Transit; Micro= Microlensing^cEquivalent Isotropic Radiated Power using the specified 1σ limit

Table 6 Known exoplanets in the survey field, from the exoplanet catalog with no known distance: <http://exoplanet.eu/>

Designation	RA (J2000) (deg.)	Dec (J2000) (deg.)	Distance (pc)	MSin(i) (M_J^a)	Period (days)	Detection method ^b	1σ RMS (Jy/beam)	EIRP ^c <10 ¹³ (W)
KMT-2017-BLG-2820	263.743	-28.548				Micro	0.15	N/A
KMT-2019-BLG-2073	267.471	-29.588		0.19		Micro	0.14	N/A
OGLE-2016-BLG-596L b	267.803	-30.850		12.20		Micro	0.15	N/A
OGLE-2017-BLG-0560	267.964	-30.459		1.90		Micro	0.15	N/A
OGLE-2019-BLG-0551	269.870	-28.841		0.02		Micro	0.15	N/A
OGLE-2012-BLG-1323	270.077	-28.584		0.01		Micro	0.15	N/A
OGLE-2016-BLG-1540	270.196	-28.360				Micro	0.14	N/A
OGLE-2016-BLG-1928	270.380	-29.130		0.00		Micro	0.15	N/A

^aMass of planet times the sine of orbit inclination, in Jupiter masses

^bRV= Radial Velocity; I=Imaging; PT=Primary Transit; Micro= Microlensing

^cEquivalent Isotropic Radiated Power using the specified 1σ limit

N/A = Not Applicable as distances are unknown

Southern Observatory VLT HAWK instrument, they determined the precise photometric properties of 3.3×10^6 stars with an assumed distance of $8178 \pm 13_{stat}$ pc (Gravity Collaboration, 2019).

The GNS infrared survey only covers 0.15% of our field and accounts for in excess of 3.3 million stars. So our blind search will likely cover billions of stars (and background galaxies). Using the distance of 8.1 kpc, we place a limit on the EIRP of putative transmitters within our observing band of $<1.1 \times 10^{19}$ W.

4 DISCUSSION

The median distance for the 144 known exoplanet systems toward the Galactic Centre is 5585 pc with the shortest distance at 39 pc. This is compared to the 28 pc for the 6 exoplanets in Tremblay & Tingay (2020), 50 pc for the 22 exoplanets examined by Tingay et al. (2018) and ≈ 2000 pc for the 45 exoplanets examined by Tingay et al. (2016). The EIRP upper limits in this paper represent some of the highest limits in our surveys to date, but as this is the first published survey in this frequency range we find this an important starting point.

There are several metrics which allow for context of the transmitter values and the potential for detecting other societies. An extrapolation of terrestrial technology from the Kardashev (Kardashev, 1964) scale, where a Type I civilisation with technology close to Earth is predicted to be able to emit a non-isotropically radiated signal at $\sim 10^{17}$ W, is one suggested method. We note that such a civilisation would only need to be able to build a big dish. Sullivan & Knowles (1985) suggest that with an Arecibo-like single dish we could detect passive radio signals (or radio leakage) out to 9 pc and with a large array of smaller dishes the distance could be more than 10 times that. Overall, they concluded the most detectable signal from another planet would be a powerful military satellite.

Using examples on Earth, especially in the frequency range of the MWA, we can look at the Air Force Space Surveillance System known as ‘‘Space Fence’’ which operated up until 2013. This system was a 1 MW continuous wave (0.1 Hz BW) system operating at 216 MHz illuminating a $120 \text{ deg} \times 1.5 \text{ arcmin}$ field at an EIRP of approximately 1.5×10^{10} W (Sullivan & Knowles, 1985). If we compare this with our upper limits for the closest source, we are still three orders of magnitude from detecting a signal of this strength.

Similar to the metric used by Sheikh et al. (2020), we could measure our limits against the Arecibo Planetary Radar experiment ($\sim 20 \times 10^{12}$ W transmitted through a 305m parabolic reflector; L_A ; Siemion et al. 2013). Their largest value for the EIRP limit for stars in 7–143 pc is an upper limit in L_A of 0.88. However, with our frequency resolution of 10 kHz and the distances of 39 pc or greater, the smallest L_A upper limit is ~ 13 . This is significantly larger than our results from our other MWA surveys, which represented a population of closer stars.

Currently the MWA is undergoing an upgrade which will be pertinent to future SETI advances. Over the next 6 months, the MWA will be upgraded to increase frequency and time resolution, which will better match the kHz and sub-kHz searches completed by other facilities. An alternative approach to narrow-band SETI, first suggested by Cole & Ekers (1979), is to search for impulsive wide-band technosignatures; however comparatively few searches have been conducted. Gajjar et al. (2021) search for artificial transient signals (0.7–194 ms duration) from the GC, using non-physical dispersion as a discriminant. Our interferometric data does not have sufficient time resolution for such a search, and at low frequencies signals are severely broadened on sight-lines (as discussed in Section 4.1) with high electron density, such as toward the GC. Nevertheless, the upgraded in higher time resolution modes which could be employed to search for impulsive low-frequency technosignatures

toward the GC or other target fields.

4.1 Spectral broadening due to intervening media

Electron density fluctuations in the interstellar medium (ISM), solar wind and interplanetary medium (IPM) cause spectral broadening by scattering signals as they are propagating through them. This is of particular concern for low-frequency observations of the GC, as the effect is stronger at low frequencies, and the large electron density fluctuations in the GC cause strong scattering. Although the MWA capabilities at the time of these observations have a relatively wide frequency resolution of 10 kHz, future upgrades planned for 2021 will allow for sub-kHz resolution. We therefore explore here the potential impact of future observations in this section.

The effect of the ISM on narrowband signals is detailed in Cordes & Lazio (1991) and Cordes et al. (1997). In the strong scattering regime a narrowband sinusoid with frequency ν_{GHz} in GHz will be broadened by

$$\Delta\nu_{\text{broad}} = 0.14 \text{ Hz } \nu_{\text{GHz}}^{-6/5} \left(\frac{V_{\perp}}{100} \right) \text{ SM}^{3/5}, \quad (2)$$

where $\Delta\nu_{\text{broad}}$ is the spectral broadening in Hz, V_{\perp} is the transverse velocity of the source in km s^{-1} , and SM is the scattering measure along the line of sight. The SM is an integrated measure of electron density fluctuations $C_{n_e}^2$ along the line of sight to a distance L , (Rickett, 1990), defined as

$$\text{SM} = \int_0^L C_{n_e}^2(z) dz. \quad (3)$$

Estimates of SM toward the GC can be found using the NE2001 Galactic electron density model (Cordes & Lazio, 2002). To estimate the spectral broadening of narrowband signals at MWA frequencies, we use the PYGEDM code (Price et al., 2021) to generate SM from NE2001 as a function of distance toward the GC (Fig. 6, left). To avoid a discontinuity at the GC ($l=0$, $b=0$), we add a 0.5 deg offset in Galactic latitude when calculating SM. The highest radial velocities within the Galaxy occur toward the GC, reaching $|V_{\perp}| \approx 280 \text{ km s}^{-1}$ (Dame et al., 2001). Applying Eq. 2, we find spectral broadening of under 7.5 Hz at an observational frequency of 150 MHz: well below our channel resolution of 10 kHz.

Following Siemion et al. (2013), spectral broadening due to the IPM can be estimated as

$$\Delta\nu_{\text{broad}} = 300 \text{ Hz } \nu_{\text{GHz}}^{-6/5} \left(\frac{R}{R_{\odot}} \right)^{-9/5} \quad (4)$$

where R_{\odot} is the radius of the Sun, and R is the solar impact distance. The $R^{-9/5}$ dependence is detailed in

Woo (2007), based on an empirical fit to spectral broadening measured from the *Pioneer* 10, 11 and *Helios* 1 space mission telemetry, and corroborated by radar reflections from Venus at superior conjunction (Harmon & Coles, 1983); this power law holds from $\sim 10R_{\odot}$ to $\sim 200R_{\odot}$. Solar activity and coronal mass ejections can nonetheless cause significant variations. Fig. 6 (right) shows the estimated effect of the IPM from Eq. 4 for MWA frequencies. The effect of the IPM can be more significant than the ISM, particularly when the solar impact distance is small (i.e., the Sun passes close to the GC with respect to Earth).

Electron density fluctuations also impart scintillation on propagating signals, the characteristic timescale of which is given by

$$\Delta t_d = 3.3 \text{ s } \nu_{\text{GHz}}^{-6/5} \left(\frac{V_{\perp}}{100} \right)^{-1} \text{ SM}^{-3/5}. \quad (5)$$

If Δt_d is much shorter than the observation length, scintillation effects will be quenched; however, if Δt_d is much longer than the observation length, the signal may be effectively amplified or attenuated by scintillation during the observation, simplifying or confounding detection above our sensitivity threshold (Cordes & Lazio, 1991). Only the two nearest known exoplanets in the survey field, HD 164604 b and HD 165155 b, have Δt_d estimates significantly larger than our 7-hr observation length (using SM derived from NE2001). These sources could be re-observed at a later date, in case of scintillation-induced attenuation.

For our observations at 150 MHz, neither ISM nor IPM-induced broadening are significant effects. However, these effects should be considered in \sim Hz frequency resolution observations at low frequencies, in particular for proposed Moon-based SETI missions at frequencies below 1 MHz (e.g. Michaud et al., 2021) and future upgrades to the MWA. Signals from exoplanets that are occulted by their host star (with respect to Earth) can have large stellar impact distances and consequently large spectral broadening. The space weather around an exoplanet's host star will also affect broadening and scintillation; we note this as a potential field for future research.

5 CONCLUSIONS

We searched sightlines toward 144 known exoplanetary systems for artificial signals, finding no plausible technosignatures above an EIRP_{min} from 10^{13} W to 10^{19} W (depending on distance to the source). We also conducted a blind survey across a 200 deg² field toward the GC, which covers billions of stars, including 3.3 million stars within 6000 pc² (0.3 deg²) of the GC from the GALACTICNUCLEUS survey. Our observations across 139–170 MHz are complementary to Tingay et al. (2013)

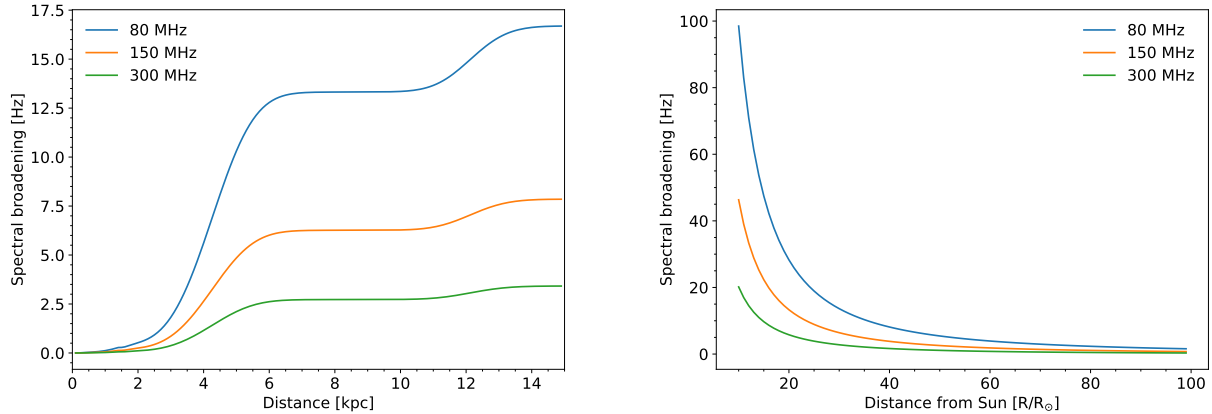


Figure 6. Estimates of spectral broadening due to the interstellar medium (left) and interplanetary medium (right), for narrowband signals propagating from the direction of the GC.

(103–133 MHz) and higher-frequency (0.7–93 GHz) technosignature searches currently underway with the Parkes and Green Bank telescopes (Gajjar et al., 2021). Combined, these observations will allow statistical limits on the prevalence of putative transmitters at radio wavelengths in the GC. Future GC observations with the MWA and other instruments could allow full frequency coverage from 80 MHz to 93 GHz. Planned improvements to the MWA, due to be online in late 2021, will provide data with finer frequency and time resolution, which will improve the MWA’s sensitivity to narrowband technosignatures and pulsating signals. Continual improvement of telescope capabilities, when combined with methodical observational campaigns, provides a means to explore the vast parameter space within which signs of technologically-capable life may be waiting to be found.

6 ACKNOWLEDGEMENTS

We thank A. Siemion and V. Gajjar for discussion on spectral broadening. We also thank the anonymous reviewers for their helpful comments and suggestions to improve the manuscript.

6.1 Facilities

This scientific work makes use of the Murchison Radio-astronomy Observatory, operated by CSIRO. We acknowledge the Wajarri Yamatji people as the traditional owners of the Observatory site. Support for the operation of the MWA is provided by the Australian Government (NCRIS), under a contract to Curtin University administered by Astronomy Australia Limited.

6.2 Computer Services

We acknowledge the Pawsey Supercomputing Centre which is supported by the Western Australian and Australian Governments. Access to Pawsey Data Storage Services is governed by a Data Storage and Management Policy (DSMP). The All-Sky Virtual Observatory (ASVO) has received funding from the Australian Commonwealth Government through the National eResearch Collaboration Tools and Resources (NeCTAR) Project, the Australian National Data Service (ANDS), and the National Collaborative Research Infrastructure Strategy. This research has made use of NASA’s Astrophysics Data System Bibliographic Services.

6.3 Software

The following software was used in the creation of the data cubes:

- AOFLAGGER and COTTER – Offringa et al. (2015)
- WSCLEAN – Offringa et al. (2014); Offringa & Smirnov (2017)
- AEGEAN – Hancock et al. (2018)
- MIRIAD – Sault et al. (1995)
- TOPCAT – Taylor (2005)
- NumPy v1.11.3 (Dubois et al., 1996), AstroPy v2.0.6 (Astropy Collaboration et al., 2013), SciPy v0.17.0 (Oliphant, 2007), Matplotlib v1.5.3 (Hunter, 2007)
- CARTA – Comrie et al. (2020)
- PYGEDM – Price et al. (2021)

REFERENCES

Astropy Collaboration Robitaille T. P., Tollerud E. J.,

- Greenfield P., Droettboom M., Bray E., et al., 2013, *A&A*, **558**, A33
- Cai X., Jiang J. H., Fahy K. A., Yung Y. L., 2021, *Galaxies*, **9**, 5
- Carroll-Nellenback J., Frank A., Wright J., Scharf C., 2019, *AJ*, **158**, 117
- Cole T. W., Ekers R. D., 1979, *PASA*, **3**, 328
- Comrie A., et al., 2020, CARTA: The Cube Analysis and Rendering Tool for Astronomy, doi:10.5281/zenodo.3377984
- Cordes J. M., Lazio T. J., 1991, *ApJ*, **376**, 123
- Cordes J. M., Lazio T. J. W., 2002, arXiv e-prints, pp astro-ph/0207156
- Cordes J. M., Lazio J. W., Sagan C., 1997, *ApJ*, **487**, 782
- Dame T. M., Hartmann D., Thaddeus P., 2001, *ApJ*, **547**, 792
- Di Stefano R., Ray A., 2016, *ApJ*, **827**, 54
- Dubois P. F., Hinsen K., Hugumin J., 1996, *Comput. Phys. Commun.*, **10**, 262
- Ellingson S. W., Clarke T. E., Cohen A., Craig J., Kassim N. E., Pihlstrom Y., Rickard L. J., Taylor G. B., 2009, *IEEE Proceedings*, **97**, 1421
- Enriquez J. E., et al., 2017, *ApJ*, **849**, 104
- Gajjar V., et al., 2021, *AJ*, **162**, 33
- Garrett M., Siemion A., van Cappellen W., 2017, arXiv e-prints, p. arXiv:1709.01338
- Gowanlock M. G., Patton D. R., McConnell S. M., 2011, *Astrobiology*, **11**, 855
- Gravity Collaboration 2019, *A&A*, **625**, L10
- Gupta Y., et al., 2017, *Current Science*, **113**, 707
- Hancock P. J., Trott C. M., Hurley-Walker N., 2018, *PASA*, **35**, e011
- Harmon J. K., Coles W. A., 1983, *ApJ*, **270**, 748
- Houston K. M., Siemion A. P. V., Croft S., 2021, arXiv e-prints, p. arXiv:2106.06594
- Hunter J. D., 2007, *Comput. Sci. Eng.*, **9**, 90
- Hurley-Walker N., Callingham J. R., Hancock P. J., Franzen T. M. O., Hindson L., et al., 2017, *MNRAS*, **464**, 1146
- Jiménez-Torres J. J., Pichardo B., Lake G., Segura A., 2013, *Astrobiology*, **13**, 491
- Kardashev N. S., 1964, *Soviet Ast.*, **8**, 217
- Lacki B. C., 2021, arXiv e-prints, p. arXiv:2106.07739
- Large M. I., Mills B. Y., Little A. G., Crawford D. F., Sutton J. M., 1981, *MNRAS*, **194**, 693
- Lineweaver C. H., Fenner Y., Gibson B. K., 2004, *Science*, **303**, 59
- Loeb A., Zaldarriaga M., 2007, *JCAP*, **2007**, 020
- Michaud E., Siemion A. P. V., Drew J., Worden S. P., 2021, in *Bulletin of the American Astronomical Society*. p. 369, doi:10.3847/25c2cfcb.19d4b457
- Morgan J., Galvin T., 2021, johns-morgan/mwa_pb_lookup: Version 1.0, doi:10.5281/zenodo.5083990, <https://doi.org/10.5281/zenodo.5083990>
- Morrison I. S., Gowanlock M. G., 2015, *Astrobiology*, **15**, 683
- Newman W. I., Sagan C., 1981, *Icarus*, **46**, 293
- Nogueras-Lara F., et al., 2018, *A&A*, **610**, A83
- Nogueras-Lara F., et al., 2019, *A&A*, **631**, A20
- Offringa A. R., Smirnov O., 2017, *MNRAS*, **471**, 301
- Offringa A. R., McKinley B., Hurley-Walker et al., 2014, *MNRAS*, **444**, 606
- Offringa A. R., Wayth R. B., Hurley-Walker N., Kaplan D. L., Barry N., et al., 2015, *PASA*, **32**, e008
- Oliphant T. E., 2007, *Comput. Sci. Eng.*, **9**, 10
- Price D. C., Deller A., Flynn C., 2021, arXiv e-prints, p. arXiv:2106.15816
- Rickett B. J., 1990, *ARA&A*, **28**, 561
- Sault R. J., Teuben P. J., Wright M. C. H., 1995, in Shaw R. A., Payne H. E., Hayes J. J. E., eds, *Astronomical Society of the Pacific Conference Series Vol. 77, Astronomical Data Analysis Software and Systems IV*. p. 433 (arXiv:astro-ph/0612759)
- Sheikh S. Z., Siemion A., Enriquez J. E., Price D. C., Isaacson H., Lebofsky M., Gajjar V., Kalas P., 2020, *AJ*, **160**, 29
- Shostak G. S., Tarter J., 1985, *Acta Astronautica*, **12**, 369
- Siemion A. P. V., et al., 2013, *ApJ*, **767**, 94
- Sokolowski M., et al., 2017, *PASA*, **34**, e062
- Sullivan W. T. I., Knowles S. H., 1985, in Papagianis M. D., ed., *Lunar reflections of terrestrial radio leakage. Vol. 112, The Search for Extraterrestrial Life: Recent Developments*. pp 327–334
- Sullivan W. T. I., Brown S., Wetherill C., 1978, *Science*, **199**, 377
- Tarter J., 2001, *ARA&A*, **39**, 511
- Taylor M. B., 2005, in Shopbell P., Britton M., Ebert R., eds, *Astronomical Society of the Pacific Conference Series Vol. 347, Astronomical Data Analysis Software and Systems XIV*. p. 29
- Tingay S. J., Goeke R., Bowman J. D., Emrich D., Ord S. M., et al., 2013, *PASA*, **30**, e007
- Tingay S. J., Tremblay C., Walsh A., Urquhart R., 2016, *ApJ*, **827**, L22
- Tingay S. J., Tremblay C. D., Croft S., 2018, *ApJ*, **856**, 31
- Tremblay C. D., Tingay S. J., 2020, *PASA*, **37**, e035
- Tremblay C. D., et al., 2020, *ApJ*, **905**, 65
- Wayth R. B., Tingay S. J., Trott C. M., Emrich D., Johnston-Hollitt M., et al., 2018, *PASA*, **35**, 33
- Woo R., 2007, *Space Weather*, **5**, S09004
- Worden S. P., et al., 2017, *Acta Astronautica*, **139**, 98
- van Haarlem M. P., et al., 2013, *A&A*, **556**, A2